I&EC research
Industrial & Engineering Chemistry Research
pubs.acs.org/IECR
Article

Charge Transport Dynamics in Microwave Synthesized One-Dimensional Molybdenum Chalcogenides

Jessica C. Ortiz-Rodríguez, Joseph T. Perryman, and Jesús M. Velázquez*

Cite This: *Ind. Eng. Chem. Res.* 2021, 60, 16153−16161
Read Online

ABSTRACT: Scalable synthesis of one-dimensional molybdenum chalcogenides with tunable electronic properties may be critical for the development of nanoscale electronic device components as well as functional energy-conversion catalysts. Herein, we report the direct synthesis of one-dimensional potassium-intercalated molybdenum chalcogenides in the pseudo-Chevrel−Phase family [$K_2Mo_6X_6$; X = S, Se, Te] through a rapid microwave-assisted solid-state heating protocol. Interfacial capacitance as well as charge transfer dynamics during aqueous proton reduction are both explored as a function of chalcogen composition. We observe a significant change in the anisotropic nucleation of these structures as the chalcogen increases in size and decreases in electronegativity from sulfur to tellurium, with the former dramatically encouraging nucleation of well-defined nanomaterials in comparison to the latter. These anisotropic structures exhibit increased specific capacitance from 2.25 F g^{-1} to 10.28 F g^{-1} as the electronegativity of the chalcogen increases (Te < Se < S). Charge transfer kinetics for proton reduction follow a similar chalcogen-dependence, with the smallest charge transfer resistance being 1.16 Ω for $K_2Mo_6S_6$ at −0.6 V vs RHE, compared to 3.7 Ω for $K_2Mo_6Te_6$ at the same potential. Results discussed herein highlight interesting composition-dependent properties that could guide the future selection and development of molybdenum chalcogenide materials.

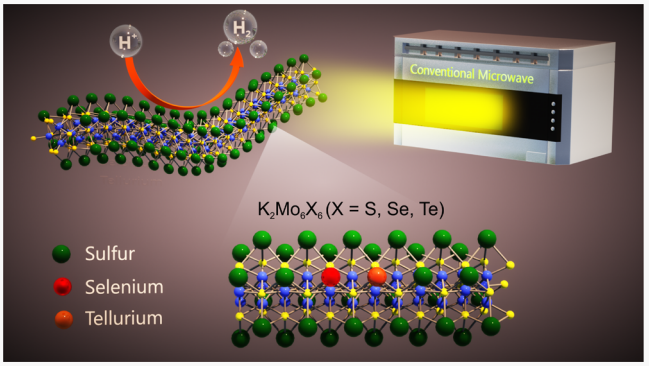

INTRODUCTION

Evolving industrial applications for functional materials are driving an increase in our need for precisely engineered compositions that exhibit favorable physicochemical properties for reactions of interest.[1−3] One approach to establishing transferrable design principles across material classes is to identify compositionally flexible frameworks to study and subsequently optimize.[4,5] Such frameworks would ideally be characterized by (i) tunable multinary compositions; (ii) modular bonding landscapes that also lend themselves to efficient synthetic protocols, allowing for fine control over dimensionality and morphology;[6] and (iii) quantifiable and application-specific functionality criteria that—in the case of heterogeneous electrocatalysis, for example—include metrics such as hydrogen adsorption affinity and interfacial resistance to charge transfer.[7−11] Identifying and investigating material families that have requisite properties for any given application will enable meaningful extraction of design principles that inform optimizations of functional atomic configurations.

To this end, metal chalcogenides are exceptionally promising, because of their readily interchangeable binary and ternary compositions, their tendency to form well-defined 0D−3D dimensionalities at different composition thresholds, as well as their proven applications in electronics,[12−16] energy conversion,[15,17−21] and energy storage.[16,19,22] While much attention has been afforded to understand composition-dependent properties in transition-metal dichalcogenides (MX_2; M = transition metal; X = S, Se, Te) in particular,[12,13,16,20,22,23] far fewer experimental investigations have been dedicated to understanding ternary chalcogenides such as the interesting one-dimensional (1D) $M_2Mo_6X_6$ (M= alkali metal; X = S, Se, Te) system, also known as pseudo-Chevrel−Phases (PCPs).[24−27] Besides the interesting properties associated with 1D systems due to electron confinement,[28−31] PCPs have been identified as alternative materials for nanodevices, because of their predicted high elasticity, stiffness, thermal stability, and conductivity.[15,32] Furthermore, properties that lend themselves to composites,[33,34] sensors,[35] and photovoltaic devices[36] have also been explored for this family of materials.

As shown in Figure 1, the PCP structure is characterized by infinite Mo_6X_6 chains separated by chalcogen-coordinated

Received: July 15, 2021
Revised: October 20, 2021
Accepted: October 22, 2021
Published: November 4, 2021

https://doi.org/10.1021/acs.iecr.1c02825
Ind. Eng. Chem. Res. 2021, 60, 16153−16161

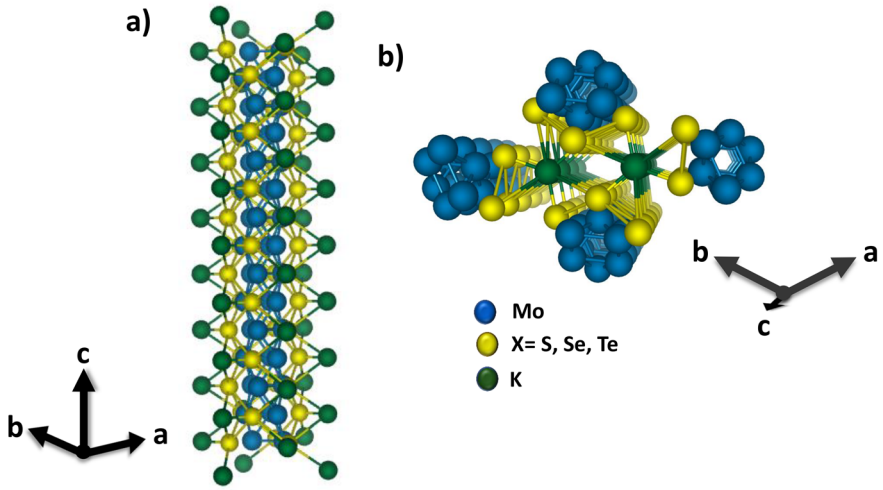

Figure 1. (a) Structure of $K_2Mo_6X_6$ depicting the 1D growth along the *c*-axis with potassium surrounding the Mo_6X_6 unit. (b) These elongated units adjoin to form hexagonal channels which are occupied by potassium.

metal intercalant ions that reside in hexagonal channels formed between adjacent Mo_6X_6 chains. Intuitively, the wirelike extended structure of these chains results in a high degree of electrical anisotropy, which has made PCPs an excellent system for studying the effect composition on electron transport in their 1D structures and evaluating fundamental properties pertinent to the design of novel nanomaterials.[15,25,26,32,37] Furthermore, the electronic properties of this ternary system can be easily tuned by changing chalcogen composition, intercalant composition, or both—making this an ideal system for studying composition−structure−function relationships. Although a variety of PCP compositions have been successfully synthesized using a various approaches,[24,27,38−44] efforts to elucidate the effect of chalcogen composition on their charge transport properties and electrochemical performance remain scarce.

Herein, we report the synthesis of potassium-intercalated PCP chalcogenides ($K_2Mo_6X_6$; X = S, Se, Te) through rapid (10 min) microwave-assisted solid-state heating, and investigate their charge-storage and electron-transfer properties as a function of changing chalcogen composition. Changes in growth kinetics and charge transport properties are correlated with anion composition in $K_2Mo_6S_6$ (S-PCP), $K_2Mo_6Se_6$ (Se-PCP), and $K_2Mo_6Te_6$ (Te-PCP), based on the results of our integrated microscopic, spectroscopic, and electroanalytical investigation. We highlight interesting performance trends in proton reduction electrocatalysis that scale directly with anion electronegativity and propose some additional elucidative spectroscopic and computational studies that will further support evolving design principles for these types of multinary chalcogenide compositions.

EXPERIMENTAL SECTION

Materials. MoS_2 powder (>95% purity, ∼325 mesh) and $MoSe_2$ powder (99.999%, ∼200 mesh) were used as purchased from Alfa Aesar. Mo powder (99.995%, ∼250 mesh), graphite rods (∼99.995%) Te powder (99.8%, ∼200 mesh), K ingot (99.95%), graphite powder (<20 μm), and concentrated H_2SO_4 acid (ACS grade) were used as purchased from Sigma−Aldrich. K_2S (>95%) was used as purchased from Pfaltz and Bauer. Al_2O_3 microfiber was used as purchased from Thermo Fisher Scientific. Fused-quartz tubes were purchased from AdValue Technology and made into round-bottom tubes with an in-house oxy-hydrogen torch. Gas diffusion media (GDL 28BC) was purchased from Ion Power. Ag/AgCl reference electrodes were purchased through ALS Japan. A Selemion anion exchange membrane was purchased from AGC Engineering and stored in ultrapure deionized (DI) water prior to use in electrochemical experiments. Ultrapure water (18.2 MΩ) was obtained with a Barnstead E-Pure filtration system.

Synthesis. The PCPs studied here were synthesized via high-temperature microwave-assisted solid-state heating, as described in our previous work.[27] Briefly, stoichiometric amounts of precursors required to achieve a stoichiometry of $K_2Mo_6X_6$; X = S, Se, Te composition were weighed in a N_2 glovebox and ball-milled under N_2 to homogenize. K_2S was used as the potassium source for the PCP sulfide because of its granular nature which facilitated the weighing process, while metallic potassium was used for the selenide and telluride phases, because of its high purity and the relative rarity of commercially available K_2Se and K_2Te. The resulting mixed precursor powders were then returned to a N_2 glovebox and pressed into pellets using a hydraulic press (Across International, 40-ton cold press). Pellets were placed in round-bottom quartz tubes and packed under N_2 using layers of Al_2O_3 microfiber and graphite. Samples were then removed from the glovebox and transferred to a graphite bath inside an alumina crucible and were irradiated in an Ar-filled conventional microwave with inverter technology (Toshiba, Model ML2EM45PAESS; 1250 W). The heating power was adjusted appropriately to maintain a temperature of ∼750 °C for 10 min, which was sufficient for synthesizing pure-phase PCPs in far less time than conventional solid-state methods.[24] Samples were then rapidly quenched in room-temperature water after the heating time.

Structural and Elemental Characterization. PCP crystal structures were evaluated via powder X-ray diffraction (PXRD) using a Bruker D8 Advance diffractometer with Cu Kα radiation (1.541 Å). Experimental lattice parameters were obtained through Pawley refinement, using the TOPAS suite from Bruker. Morphology was evaluated via scanning electron microscopy (SEM) using an FEI Nova NanoSEM 430, and bulk composition was analyzed via energy-dispersive X-ray spectroscopy (EDX), using an FEI Scios Dual Beam FIB/SEM

https://doi.org/10.1021/acs.iecr.1c02825
Ind. Eng. Chem. Res. 2021, 60, 16153−16161

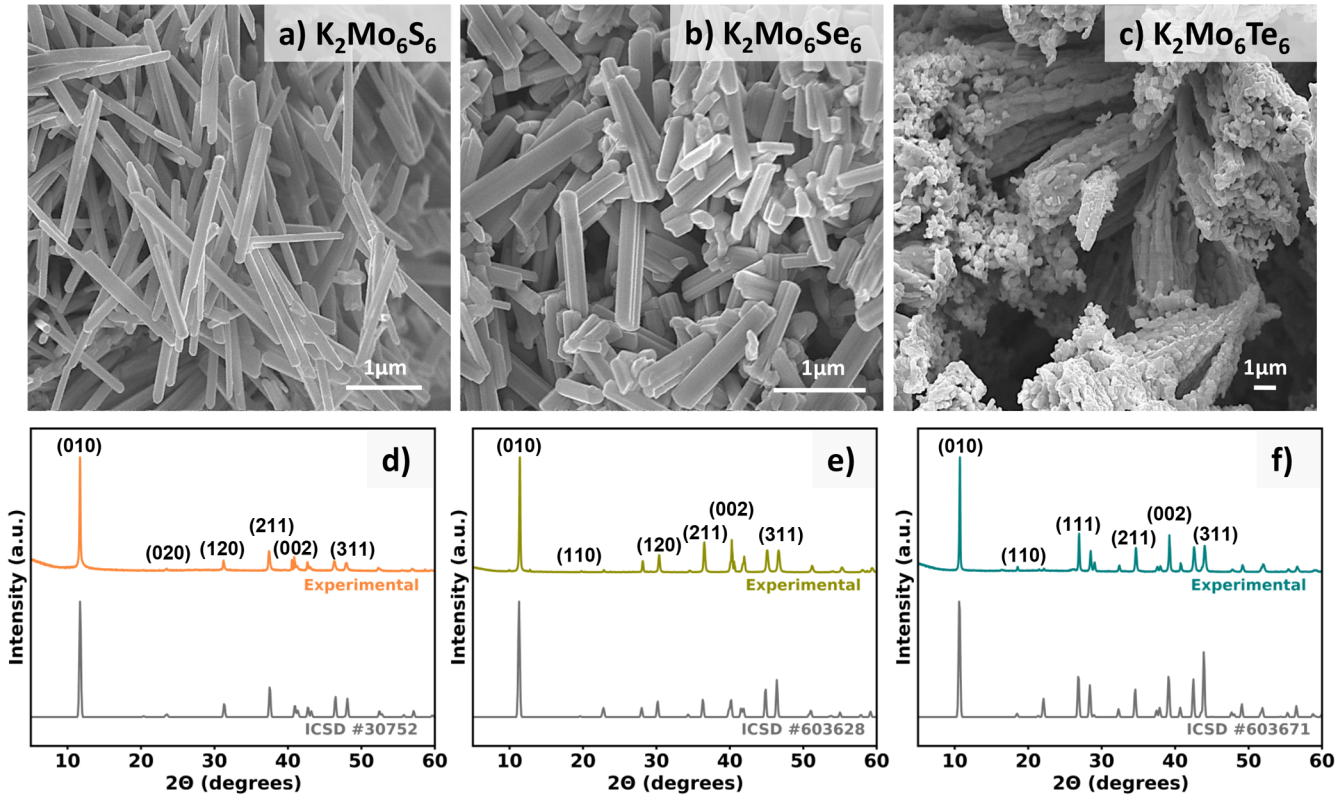

Figure 2. SEM micrographs for as-synthesized PCP (a) sulfide, (b) selenide, and (c) telluride, alongside their corresponding PXRD patterns. Experimental diffractograms are overlaid with literature patterns from the International Crystal Structure Database (ICSD) for (d) S-PCP, (e) Se-PCP, and (f) Te-PCP.

system with an Oxford EDX detector. Surface composition was analyzed via X-ray photoelectron spectroscopy (XPS), using a Kratos Supra Axis spectrometer with an Al anode (1486.6 eV). Scanning transmission electron microscopy (STEM). was performed using an aberration-corrected JEOL Model JEM-2100F system. Images were acquired using an accelerating voltage of 200 kV. Raman spectra were recorded using a Renishaw confocal Raman microscope that was equipped with a 1800 lines/mm grating and a 785 nm laser.

Electrochemical Characterization. Electrochemical measurements were performed using a Bio-Logic VSP-300 potentiostat in a three-electrode H-cell configuration, in which the counter and working electrode were separated by a Selemion ion exchange membrane. All measurements were taken in an aqueous H_2-sparged 0.5 M H_2SO_4 electrolyte, with a Ag/AgCl (3 M NaCl) reference electrode and graphite rod counter electrode. Potentials were converted to RHE scale using the following equation:

$$E_{RHE} = E(Ag/AgCl) + 0.210 + 0.059 \times pH$$

Working electrodes were prepared by depositing 15 μL of PCP ink onto a 1 cm × 2 cm microporous layer of carbon paper, followed by drying under vacuum overnight. Deposited inks consisted of the appropriate PCP powder, conductive carbon black to improve electrical connectivity, polytetrafluoroethylene (PTFE) suspension as a binding agent, and isopropyl alcohol as a solvent. Inks were sonicated for 20 min prior to being drop cast onto the carbon paper. Blank electrodes were prepared as controls through the same method, albeit without including any PCP powder. The H_2SO_4 electrolyte was deoxygenated prior to each experiment by purging with H_2 for ∼30 min.

Specific capacitance measurements were made via cyclic voltammetry (CV) in a static solution by sweeping the potential across a non-Faradaic region (∼100 mV potential window centered around the open-circuit potential) at progressively increasing scan rates. A plot of charging current as a function of scan rate yields a linear response, from which per-gram specific capacitance is obtained by dividing slope by electrode mass loading. Subsequently, proton reduction behavior was evaluated via linear sweep voltammetry (LSV) at a scan rate of 5 mV/s under vigorous stirring to mitigate mass transport limitations. Charge-transfer resistance was measured via electrochemical impedance spectroscopy (EIS) at different applied potentials, with a superimposed AC bias oscillating at frequencies ranging from 1 MHz to 1 Hz with a 10 mV sinus amplitude. Charge-transfer resistance is taken as the difference between x-intercepts of the resulting semicircular Nyquist impedance plots.

RESULTS AND DISCUSSION

We have expanded our previously reported synthetic protocol for inducing direct, solid-state nucleation of alkali-intercalated S-PCP[27] to the potassium-intercalated Se-PCP and Te-PCP also studied here. Figures 2a–c show the morphologies that were obtained through our template-free microwave-assisted approach, while the PXRD patterns for each phase are depicted in Figures 2d–f below each corresponding SEM image. An agglomeration of the crystalline structures is observed, which is typical of template-free synthesis approaches for PCPs, because

https://doi.org/10.1021/acs.iecr.1c02825
Ind. Eng. Chem. Res. 2021, 60, 16153−16161

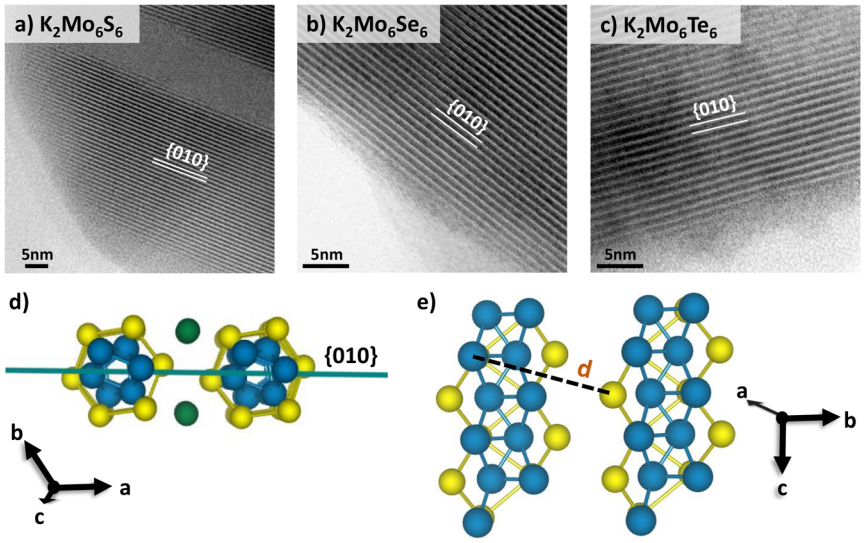

Figure 3. Bright-field STEM images for (a) S-PCP, (b) Se-PCP, and (c) Te-PCP. The observed lattice *d*-spacing for each PCP corresponds to the Mo−X distance between adjacent 1D clusters along the {010} family of planes (see panels (d) and (e)).

of intermolecular interactions between individual crystals.[27,45,46] High-resolution images of the 1D structures are included in Figure S1 in the Supporting Information. Lattice parameters obtained through Pawley refinement of the PXRD patterns agree with the previously reported hexagonal crystal structure and $P6_3/m$ space group for each PCP (see Figure S2 and Table S1 in the Supporting Information). The unit-cell parameters obtained from Pawley refinement show an expansion of the unit cell in all directions, as a function of chalcogen (S < Se < Te). Figure S3 in the Supporting Information shows the typical unit cell of PCPs, which makes it evident that the observed increases in the *a* and *b* lattice parameters, as a function of chalcogen, are associated with longer intercluster distances between Mo_6X_6. This, in turn, agrees with the observed left shift of the prominent (010) diffraction peak from S-PCP to Te-PCP (Figure S4 in the Supporting Information). Similarly, the expansion of the unit cell in the *c*-direction is associated with an increase in the Mo−Mo and X-X intracluster distances. However, the smaller change in the *c* lattice parameter, as a function of chalcogen, corresponds to a more subtle change in intramolecular distances, as compared to intermolecular distances.[47]

The Raman spectra of PCP chalcogenides show similar vibrational modes for all of the materials studied (Figure S5 in the Supporting Information). As shown in Table S2 in the Supporting Information, most of the Raman-active modes calculated for PCPs are associated with vibrations that involve atoms in 6*h* Wyckoff positions (Mo, X). The similarity in Raman shift for all PCPs studied here, in conjunction with relatively small variations in Mo−Mo distances as a function of chalcogen, could suggest that the observed Raman modes arise from Mo−Mo breathing modes which have been assigned in previous literature.[43,44,48] Nevertheless, additional modeling is needed to deconvolute the corresponding Raman vibration modes.[43,44,48] All the PCPs evaluated exhibit pronounced 1D growth, which agrees with the predominance of exposed {010} facets parallel to the hexagonal *c*-axis, as observed via STEM (Figure 3). This agrees with computational lattice energy calculations that were performed and evaluated in our previous work for S-PCP,[27] where facets parallel to the hexagonal axis had significantly lower surface energies, relative to nonparallel surfaces (Table S3 in the Supporting Information). Additional lattice planes observed for the synthesized PCP chalcogenides are included in Figures S6 and S7 in the Supporting Information.

A significant morphology change is observed for Te-PCP, compared to its sulfide and selenide analogues, as the telluride exhibits far less preferential 1D growth. Figure S7c in the Supporting Information shows a change in the exposed lattice from {010} to {001} within Te-PCP at an ∼45° angle. The change in exposed facets could be indicative of competing growth orientations, which may explain the less well-defined 1D morphology of Te-PCP. However, the observed change in morphology could also stem from changes in potassium−chalcogen interactions, which have been identified to play a role in the distance between adjacent Mo_6X_6 chains in ternary PCPs.[24,49,50] Based on this theory, the repulsive $Mo_6X_6^-$ chains are held together by ionic interactions with the ternary metal. As shown in Figure S8 in the Supporting Information, there is an overall increase in the Mo_6X_6—K bonds in Te-PCP, compared to the S-PCP, which could hinder the stabilization of the 1D structure and lead to the less-defined chains observed for Te-PCP.

Bulk PCP compositions were confirmed by EDX, where no impurities were identified for any material studied (Figure S9 in the Supporting Information). Similar results were obtained through XPS measurements, where only the corresponding elements, a native oxide layer, and adventitious carbon were identified at the surface of each PCP studied (see Figures S10−S12 in the Supporting Information). The atomic percentages obtained by EDX for Se-PCP and Te-PCP agree with the expected 1:1 molybdenum-to-chalcogen ratio. For S-PCP, the Mo L- and S K-edges overlap, convoluting quantitative determination of Mo and S. Hence, reported atomic percentages appear to deviate significantly from expected values. Potassium quantification via EDX point scans yields atomic percent compositions between 12.31% and 12.98%, which is in good statistical agreement with a nominal composition of $K_2Mo_6S_6$.

Voltammetric characterization of the materials in their respective non-Faradaic regions shows that their specific capacitance is chalcogen-dependent and increases substantially

https://doi.org/10.1021/acs.iecr.1c02825
Ind. Eng. Chem. Res. 2021, 60, 16153−16161

as the electronegativity of the chalcogen increases. S-PCP exhibited the highest ability to store charge, with a specific capacitance of 10.28 ± 0.89 F g^{-1}, compared to Se-PCP and Te-PCP at 4.20 ± 1.03 F g^{-1} and 2.25 ± 0.42 F g^{-1}, respectively (Figure 4). The electrochemical response of PCPs

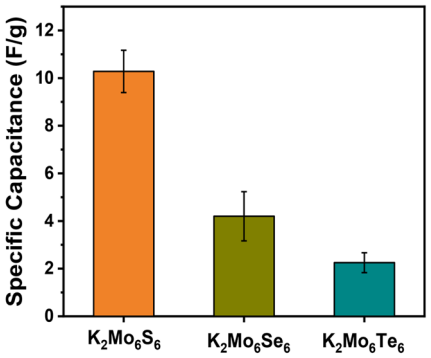

Figure 4. Specific capacitance per gram of each PCP studied.

in scanning from a non-Faradaic to a Faradaic region was evaluated via EIS under progressively more reductive potentials. Figure 5 shows the Nyquist plot for each PCP acting as the working electrode material. A double-layer charging response is observed at low potentials, as evidenced by the lack of an observable second *x*-axis intercept, while single-electron charge-transfer events along the proton reduction reaction mechanism are observable by the semicircular Nyquist plots from −0.2 V to −0.6 V vs RHE. These semicircular Nyquist plots also indicate that interfacial electron transfer can be modelled by a simple Randle's circuit involving a double-layer capacitive element, a charge-transfer-resistance element, and a circuit resistance element (see Figure S13 in the Supporting Information).

Shown in the inset of Figure 5a, individual S-PCP Nyquist plots at each negative potential are characterized by a small potential-independent semicircle at high frequencies (left semicircle) and a larger, potential-dependent semicircle at low frequencies (right semicircle). The potential-independent semicircle is associated with resistance at the interface between the carbon paper electrode and the PCP layer.[51,52] This potential-independent semicircle is less pronounced for Se-PCP and Te-PCP (Figures 5b and 5c), which indicates better contact between the electrode and may be a result of their increased lateral thickness. The potential-dependent semicircle is characteristic of a charge-transfer process.[53] An increase in the ability to transfer charge to adsorbed H* is observed for all PCPs at more reductive potentials, which is expected since surface electrons are more energetic under these conditions and are therefore more likely to transfer to unoccupied orbitals of the adsorbed species. Figure 5d shows the charge-transfer resistance (R_{ct}) of all PCPs at different potentials. The R_{ct} value of all PCPs decreased as the reductive potential was increased from −0.4 V to −0.6 V vs RHE, decreasing from 1.77 Ω to 1.16 Ω for S-PCP, 6.18 Ω to 2.16 Ω for Se-PCP, and 10.2 Ω to 3.7 Ω for Te-PCPC. S-PCP shows the highest tendency to reduce protons, evidenced by its lower R_{ct} compared to Se-PCP and Te-PCP at every potential evaluated. This trend in R_{ct} may result from a gradual metal-to-semiconductor transition for PCPs as chalcogen electronegativity decreases, as has been computationally predicted.[54,55] In other words, intrinsic electrical conductivity differences between S-PCP, Se-PCP, and Te-PCP appear to contribute significantly to the observed interfacial reactivity for proton reduction.

R_{ct} values correlate with the lower onset potential of S-PCP to generate H_2, which is shown in Figure 6a. A steady increase in the overpotential required to achieve a current density of 10 mA cm^{-2} is observed, across the series of alkali-intercalated PCPs, with overpotentials of 203.3 mV, 316.8 mV, and 347.9 mV for S-PCP, Se-PCP, and Te-PCP, respectively. Tafel slope analysis (Figure 6b) suggest that all PCPs follow a Volmer–Heyrovsky mechanism, where electrochemical desorption via proton-coupled electron transfer is the final step toward H_2 production.[56] Interestingly, the trend in increasing proton

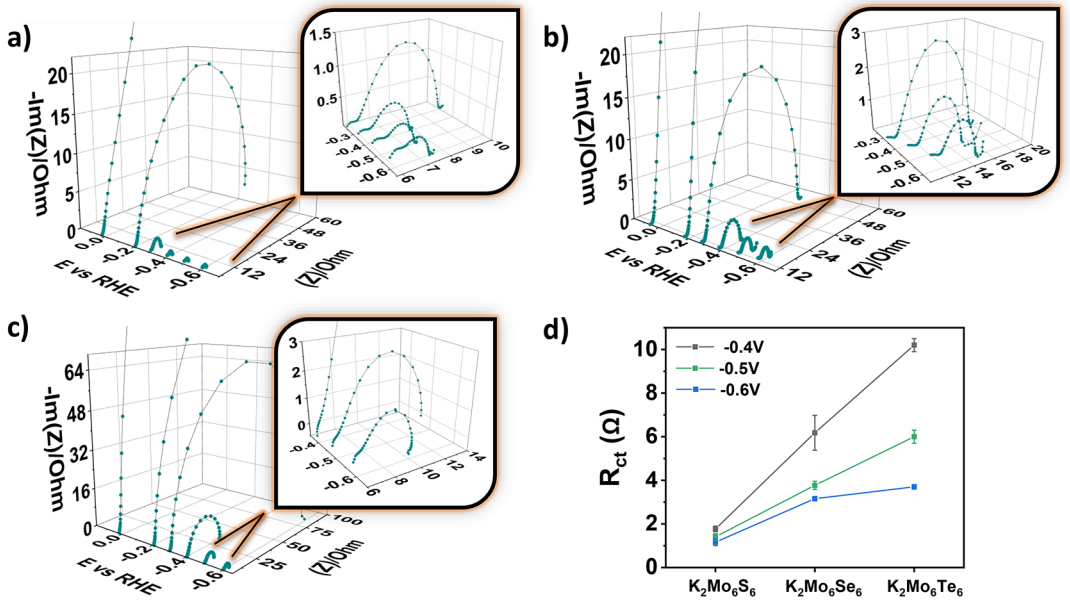

Figure 5. Nyquist plots for (a) S-PCP, (b) Se-PCP, and (c) Te-PCP at different potentials in a 0.5 M H_2SO_4 solution. (d) Charge-transfer resistance for proton reduction over all three PCPs studied, extracted from Nyquist plots.

https://doi.org/10.1021/acs.iecr.1c02825
Ind. Eng. Chem. Res. 2021, 60, 16153−16161

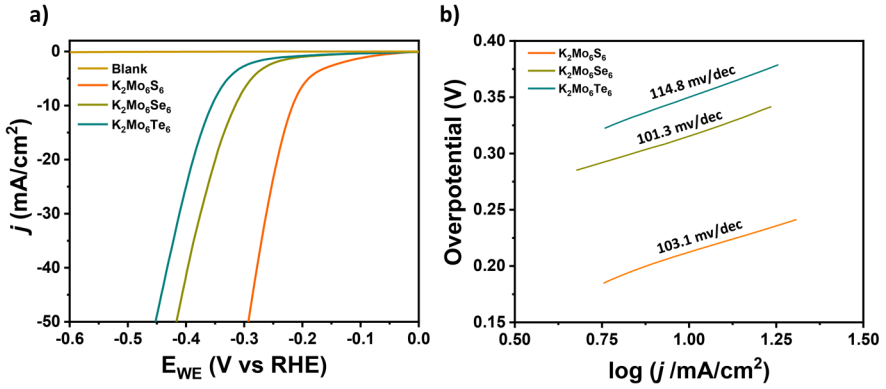

Figure 6. (a) Polarization curves for PCP electrodes in 0.5 M H_2SO_4, along with a blank for comparison. (b) Tafel plots for PCP chalcogenides illustrating the current−potential response of each ink acting as a catalyst for proton reduction.

reduction activity for the PCPs studied here as chalcogen electronegativity increases is similar to that obtained by evaluating the proton adsorption stabilization in binary Mo_6X_8 (X = S, Se, Te) Chevrel−Phases in our previous work,[11] which indicates that a similar H* adsorption configuration at Mo−X bridging sites may be stable within the PCP framework. Combining computation with experimentation in our previous work on binary Chevrel−Phases, we showed that a more electronegative chalcogen stabilizes H* adsorption more effectively due to improved X−H orbital overlap interactions, which is likely to apply to PCP chalcogenides as well.

Considering the observable change in PCP morphology from a well-defined 1D sulfide to a pseudo-3D telluride, the observed trend changes in proton reduction activity could also be associated with a decrease in the relative number of exposed active sites per unit of exposed surface area. Hence, it will be beneficial to pinpoint the adsorption position of H* on each PCP, so that exact active site densities per unit area can be compared. However, this will require a detailed computational analysis across several surface facets that also incorporates biasing and solvation effects to ascertain adsorption geometries and energetics; therefore, such an analysis is excluded from the present work.

The results of EIS are consistent with the observed performances of each PCP as a proton reduction electrocatalyst, indicating that charge transfer is a critical factor determining their interfacial reactivity. While S-PCP is the most promising electrocatalyst from an energy-input perspective (203.3 mV overpotential), the higher interfacial R_{ct} value observed for Te-PCP (3.7 Ω at −0.6 V vs RHE) makes this composition more promising as an aqueous capacitor or as a component in systems wherein aqueous hydrogen generation is undesirable.

CONCLUSION

In this work, we report the expansion of microwave-assisted solid-state synthesis to 1D selenide- and pseudo-3D telluride-based PCP chalcogenides. Template-free preferential growth exposing the {010} surface was observed for all three ternary compositions studied, while chalcogen-dependent morphology changes are explained by the observation of competitive stabilization of {010} and {001} facets in the Te-PCP, as well as the reduction of chalcogen−potassium interactions in telluride PCPs. The double-layer capacitance, charge-transfer resistance, and proton reduction reactivity of three potassium-intercalated PCP chalcogenides were all quantified in this work. The sulfide PCP displayed the highest charge storage capacity, as well as faster charge-transfer behavior during proton reduction. Decreases in charge storage capacities and R_{ct} were observed as the electronegativity of the chalcogen decreased, which agrees well with previous surface-proton interactions over analogous Chevrel−Phase materials.[11] In future studies of this interesting 1D system to elucidate electronic versus morphological driving forces for proton reduction, fine control of particle size and shape should be coupled with a rigorous computational evaluation of surface-proton interactions. A similarly rigorous interrogation of surface-localized electronic states in each PCP structure during electrochemical analysis via ex-situ and operando X-ray absorption spectroscopy will also illuminate the nature of frontier orbitals that contribute to H* adsorption and reduction. These avenues of future studies will compound on the composition−structure−function relationships discussed herein and will potentially unravel novel reactivity in this underexplored, dimensionally reduced chalcogenide composition space.

ASSOCIATED CONTENT

Supporting Information

The Supporting Information is available free of charge at https://pubs.acs.org/doi/10.1021/acs.iecr.1c02825.

High-resolution SEM micrographs for all three PCP chalcogenides, Pawley refinement for PCPs along lattice parameters obtained from refinement, PCP chalcogenides unit cell, changes in 2θ values for the diffraction peak in the (010) plane for PCP chalcogenides, Raman spectra of PCP chalcogenides, additional STEM for PCP chalcogenides, PCPs unit cell showing the changes in X−K and K−K distances, as a function of chalcogen, EDS/XPS spectra for all PCP chalcogenides, Randle's circuit used to interpret the Nyquist plots of all three PCP chalcogenides, Raman active modes for the space group $P63/m$ (No. 176) (PDF)

AUTHOR INFORMATION

Corresponding Author

Jesús M. Velázquez − *Department of Chemistry, University of California Davis, Davis, California 95616, United States;* orcid.org/0000-0003-2790-0976; Email: jevelazquez@ucdavis.edu

https://doi.org/10.1021/acs.iecr.1c02825
Ind. Eng. Chem. Res. 2021, 60, 16153−16161

Authors

Jessica C. Ortiz-Rodríguez − *Department of Chemistry, University of California Davis, Davis, California 95616, United States;* orcid.org/0000-0002-1506-5654

Joseph T. Perryman − *Department of Chemistry, University of California Davis, Davis, California 95616, United States*

Complete contact information is available at: https://pubs.acs.org/10.1021/acs.iecr.1c02825

Author Contributions

J.C.O.-R. performed the synthesis and characterization, created figures, and wrote the manuscript. J.T.P. helped perform materials characterization and edit the manuscript. J.M.V. guided the project and edit the manuscript. All authors have reviewed, edited, and given approval to the final version of the manuscript.

Funding

We would like to thank the University of California, Davis for start-up funding, as well as support from the Cottrell Scholar program supported by the Research Corporation for Science Advancement (No. RCSA 26780). J.M.V. also acknowledges funding support from the NSF through the Faculty Early Career Development Program (No. DMR-2044403). J.C.O.-R. was funded by the National Science Foundation Graduate Research Fellowship (No. NSF 1650042). Part of this work was performed at the Stanford Nano Shared Facilities (SNSF)/Stanford Nanofabrication Facility (SNF), supported by the National Science Foundation under Award No. ECCS-1542152. XPS analysis at UC Davis was supported by the National Science Foundation (No. DMR-1828238).

Notes

The authors declare no competing financial interest.

Biographies

Jessica C. Ortiz-Rodríguez is a Ph.D. candidate in the Department of Chemistry at the University of California, Davis. She received a B.S. in Chemistry from the University of Puerto Rico at Cayey in 2018, the year she also became an NSF GRFP fellow. Her research focuses on the synthesis, characterization, and electrochemical evaluation of molybdenum chalcogenides for various energy conversion reactions, such as hydrogen evolution and CO_2 reduction. She has been specifically interested in tuning the electronic structure of molybdenum chalcogenides with the goal of generating design principles for improved energy conversion electrocatalysts.

Joseph T. Perryman is a postdoctoral researcher at the SUNCAT Center for Interface Science and Catalysis, a partnership between Stanford University and SLAC National Accelerator Laboratory. He received a B.S in Chemistry and Mathematics from Linfield College in 2016. He received his Ph.D. in chemistry from the University of California at Davis in 2021, where his research focused on the synthesis, characterization, and stability analysis of multinary mixed-metal chalcogenide energy conversion catalysts.

Jesús M. Velázquez is an assistant professor of chemistry at the University of California at Davis. He received a B.S. in Chemistry from the University of Puerto Rico, Cayey, in 2004 before working as a chemist in pharmaceutical industries until 2007. In 2012, he received a Ph.D. in Chemistry from SUNY-Buffalo, under the supervision of Prof. Sarbajit Banerjee, and began working as a Ford Foundation Postdoctoral Fellow at the California Institute of Technology under the mentorship of Prof. Nathan S. Lewis. His research program is focused on the synthesis and characterization of materials that have potential to afford transformative solutions to contemporary, globally impactful energy and environmentally related problems. Current research efforts connect solid-state material synthesis and ex situ and operando spectroscopy and microscopy, as well as electrochemical analysis, in order to construct composition−structure−function relationships in multinary systems.

■ ACKNOWLEDGMENTS

We gratefully acknowledge Brian Wuille Bille for assisting in the preparation of TEM grids and acquisition of Raman spectra for all PCP chalcogenides. We thank Andrew Thron for the acquisition of STEM images. This invited contribution is part of the *I&EC Research* special issue for the 2021 Class of Influential Researchers.

REFERENCES

(1) Davis, S. J.; Lewis, N. S.; Shaner, M.; Aggarwal, S.; Arent, D.; Azevedo, I. L.; Benson, S. M.; Bradley, T.; Brouwer, J.; Chiang, Y. M.; Clack, C. T. M.; Cohen, A.; Doig, S.; Edmonds, J.; Fennell, P.; Field, C. B.; Hannegan, B.; Hodge, B. M.; Hoffert, M. I.; Ingersoll, E.; Jaramillo, P.; Lackner, K. S.; Mach, K. J.; Mastrandrea, M.; Ogden, J.; Peterson, P. F.; Sanchez, D. L.; Sperling, D.; Stagner, J.; Trancik, J. E.; Yang, C. J.; Caldeira, K. Net-Zero Emissions Energy Systems. *Science* **2018**, *360* (6396), eaas9793.

(2) Seh, Z. W.; Kibsgaard, J.; Dickens, C. F.; Chorkendorff, I.; Nørskov, J. K.; Jaramillo, T. F. Combining Theory and Experiment in Electrocatalysis: Insights into Materials Design. *Science* **2017**, *355* (6321), eaad4998.

(3) Soriaga, M. P.; Baricuatro, J. H.; Cummins, K. D.; Kim, Y. G.; Saadi, F. H.; Sun, G.; McCrory, C. C. L.; McKone, J. R.; Velazquez, J. M.; Ferrer, I. M.; Carim, A. I.; Javier, A.; Chmielowiec, B.; Lacy, D. C.; Gregoire, J. M.; Sanabria-Chinchilla, J.; Amashukeli, X.; Royea, W. J.; Brunschwig, B. S.; Hemminger, J. C.; Lewis, N. S.; Stickney, J. L. Electrochemical Surface Science Twenty Years Later: Expeditions into the Electrocatalysis of Reactions at the Core of Artificial Photosynthesis. *Surf. Sci.* **2015**, *631*, 285−294.

(4) Wang, C.; Liu, D.; Lin, W. Metal-Organic Frameworks as a Tunable Platform for Designing Functional Molecular Materials. *J. Am. Chem. Soc.* **2013**, *135* (36), 13222−13234.

(5) Singstock, N. R.; Ortiz-Rodríguez, J. C.; Perryman, J. T.; Sutton, C.; Velázquez, J. M.; Musgrave, C. B. Machine Learning Guided Synthesis of Multinary Chevrel Phase Chalcogenides. *J. Am. Chem. Soc.* **2021**, *143* (24), 9113−9122.

(6) Levi, E.; Aurbach, D. Chevrel Phases, $M_xMo_6T_8$ (M = Metals, T = S, Se, Te) as a Structural Chameleon: Changes in the Rhombohedral Framework and Triclinic Distortion. *Chem. Mater.* **2010**, *22* (12), 3678−3692.

(7) Jiao, Y.; Zheng, Y.; Davey, K.; Qiao, S. Z. Activity Origin and Catalyst Design Principles for Electrocatalytic Hydrogen Evolution on Heteroatom-Doped Graphene. *Nat. Energy* **2016**, *1*, 16130.

(8) Koper, M. T. M. Thermodynamic Theory of Multi-Electron Transfer Reactions: Implications for Electrocatalysis. *J. Electroanal. Chem.* **2011**, *660* (2), 254−260.

(9) Peng, Y.; Lu, B.; Wang, N.; Li, L.; Chen, S. Impacts of Interfacial Charge Transfer on Nanoparticle Electrocatalytic Activity towards Oxygen Reduction. *Phys. Chem. Chem. Phys.* **2017**, *19* (14), 9336−9348.

(10) Göttle, A. J.; Koper, M. T. M. Proton-Coupled Electron Transfer in the Electrocatalysis of CO_2 Reduction: Prediction of Sequential vs. Concerted Pathways Using DFT. *Chem. Sci.* **2017**, *8* (1), 458−465.

(11) Ortiz-Rodríguez, J. C.; Singstock, N. R.; Perryman, J. T.; Hyler, F. P.; Jones, S. J.; Holder, A. M.; Musgrave, C. B.; Velázquez, J. M. Stabilizing Hydrogen Adsorption through Theory-Guided Chalcogen Substitution in Chevrel-Phase Mo_6X_8 (X = S, Se, Te) Electrocatalysts. *ACS Appl. Mater. Interfaces* **2020**, *12* (32), 35995−36003.

(12) Manzeli, S.; Ovchinnikov, D.; Pasquier, D.; Yazyev, O. V.; Kis, A. 2D Transition Metal Dichalcogenides. *Nat. Rev. Mater.* **2017**, *2*, 17033.

(13) Huang, W.; Gan, L.; Li, H.; Ma, Y.; Zhai, T. 2D Layered Group IIIA Metal Chalcogenides: Synthesis, Properties and Applications in Electronics and Optoelectronics. *CrystEngComm* **2016**, *18* (22), 3968−3984.

(14) Heine, T. Transition Metal Chalcogenides: Ultrathin Inorganic Materials with Tunable Electronic Properties. *Acc. Chem. Res.* **2015**, *48*, 65−72.

(15) Shang, C.; Fu, L.; Zhou, S.; Zhao, J. Atomic Wires of Transition Metal Chalcogenides: A Family of 1D Materials for Flexible Electronics and Spintronics. *JACS Au* **2021**, *1* (2), 147−155.

(16) Han, S. A.; Bhatia, R.; Kim, S. W. Synthesis, Properties and Potential Applications of Two-Dimensional Transition Metal Dichalcogenides. *Nano Convergence* **2015**, *2* (17), 1−14.

(17) Voiry, D.; Shin, H. S.; Loh, K. P.; Chhowalla, M. Low-Dimensional Catalysts for Hydrogen Evolution and CO_2 Reduction. *Nat. Rev. Chem.* **2018**, *2* (1), 0105.

(18) Tang, Z.; Yang, H. Transition Metal Chalcogenides for Energy Storage and Conversion. In *Advanced Nanomaterials for Electrochemical-Based Energy Conversion and Storage*; Ran, F., Chen, S., Eds.; Elsevier, 2019; pp 355−391.

(19) Zhang, Y.; Zhou, Q.; Zhu, J.; Yan, Q.; Dou, S. X.; Sun, W. Nanostructured Metal Chalcogenides for Energy Storage and Electrocatalysis. *Adv. Funct. Mater.* **2017**, *27* (35), 1702317.

(20) Fu, Q.; Han, J.; Wang, X.; Xu, P.; Yao, T.; Zhong, J.; Zhong, W.; Liu, S.; Gao, T.; Zhang, Z.; Xu, L.; Song, B. 2D Transition Metal Dichalcogenides: Design, Modulation, and Challenges in Electrocatalysis. *Adv. Mater.* **2021**, *33* (6), 1907818.

(21) Perryman, J. T.; Ortiz-Rodriguez, J. C.; Jude, J. W.; Hyler, F. P.; Davis, R. C.; Mehta, A.; Kulkarni, A. R.; Patridge, C. J.; Velazquez, J. M. Metal-Promoted Mo_6S_8 Clusters: A Platform for Probing Ensemble Effects on the Electrochemical Conversion of CO_2 and CO to Methanol. *Mater. Horiz.* **2020**, *7*, 193−202.

(22) Zhang, Y.; Zhang, L.; Lv, T.; Chu, P. K.; Huo, K. Two-Dimensional Transition Metal Chalcogenides for Alkali Metal Ions Storage. *ChemSusChem* **2020**, *13* (6), 1114−1154.

(23) Hu, Z.; Wu, Z.; Han, C.; He, J.; Ni, Z.; Chen, W. Two-Dimensional Transition Metal Dichalcogenides: Interface and Defect Engineering. *Chem. Soc. Rev.* **2018**, *47* (9), 3100−3128.

(24) Tarascon, J. M.; Hull, G. W.; DiSalvo, F. J. A Facile Synthesis of Pseudo One-Monodimensional Ternary Molybdenum Chalcogenides $M_2Mo_6X_6$ (X = Se,Te; M = Li,Na..Cs). *Mater. Res. Bull.* **1984**, *19* (7), 915−924.

(25) Tarascon, J. M.; DiSalvo, F. J.; Waszczak, J. V. Physical Properties of Several $M_2Mo_6X_6$ Compounds (M = Group IA Metal; X = Se, Te). *Solid State Commun.* **1984**, *52* (3), 227−231.

(26) Hor, P. H.; Meng, R. L.; Chu, C. W.; Tarascon, J. M.; Wu, M. K. High Pressure Study on Quiasi-One-Dimensional Compounds $M_2Mo_6X_6$. *Physica B+C* **1985**, *135* (1), 245−247.

(27) Perryman, J. T.; Kulkarni, A. R.; Velázquez, J. M. Direct Solid-State Nucleation and Charge-Transport Dynamics of Alkali Metal-Intercalated $M_2Mo_6S_6$ (M = K, Rb, Cs) Nanorods. *J. Mater. Chem. C* **2020**, *8* (31), 10742−10748.

(28) Machín, A.; Fontánez, K.; Arango, J. C.; Ortiz, D.; De León, J.; Pinilla, S.; Nicolosi, V.; Petrescu, F. I.; Morant, C.; Márquez, F. One-Dimensional (1D) Nanostructured Materials for Energy Applications. *Materials* **2021**, *14* (10), 2609.

(29) Weng, B.; Liu, S.; Tang, Z. R.; Xu, Y. J. One-Dimensional Nanostructure Based Materials for Versatile Photocatalytic Applications. *RSC Adv.* **2014**, *4* (25), 12685−12700.

(30) Pantano, M. F.; Kuljanishvili, I. Advances in Mechanical Characterization of 1D and 2D Nanomaterials: Progress and Prospects. *Nano Express* **2020**, *1* (2), 022001.

(31) Arrabito, G.; Aleeva, Y.; Ferrara, V.; Prestopino, G.; Chiappara, C.; Pignataro, B. On the Interaction between 1d Materials and Living Cells. *J. Funct. Biomater.* **2020**, *11* (2), 40.

(32) Çakir, D.; Durgun, E.; Gülseren, O.; Ciraci, S. First Principles Study of Electronic and Mechanical Properties of Molybdenum Selenide Type Nanowires. *Phys. Rev. B: Condens. Matter Mater. Phys.* **2006**, *74* (23), 235433.

(33) Golden, J. H.; DiSalvo, F. J.; Fréchet, J. M. J.; Silcox, J.; Thomas, M.; Elman, J. Subnanometer-Diameter Wires Isolated in a Polymer Matrix by Fast Polymerization. *Science* **1996**, *273* (5276), 782−784.

(34) Chin, S. J.; Hornsby, P.; Vengust, D.; Mihailović, D.; Mitra, J.; Dawson, P.; Mcnally, T. Composites of Poly(ε-Caprolactone) and $Mo_6S_3I_6$ Nanowires. *Polym. Adv. Technol.* **2012**, *23* (2), 149−160.

(35) Qi, X.; Osterloh, F. E. Chemical Sensing with $LiMo_3Se_3$ Nanowire Films. *J. Am. Chem. Soc.* **2005**, *127* (21), 7666−7667.

(36) Majkić, A.; Gadermaier, C.; Celic, N.; Topolovsek, P.; Bratina, G.; Mihailovic, D. $Mo_6S_{9-X}Ii_X$ Nanowires as Additives for Enhanced Organic Solar Cell Performance. *Sol. Energy Mater. Sol. Cells* **2014**, *127*, 63−66.

https://doi.org/10.1021/acs.iecr.1c02825
Ind. Eng. Chem. Res. 2021, 60, 16153−16161

(37) Jin, K. H.; Liu, F. 1D Topological Phases in Transition-Metal Monochalcogenide Nanowires. *Nanoscale* **2020**, *12* (27), 14661−14667.
(38) Zhu, H.; Wang, Q.; Zhang, C.; Addou, R.; Cho, K.; Wallace, R. M.; Kim, M. J. New Mo_6Te_6 Sub-Nanometer-Diameter Nanowire Phase from 2H-$MoTe_2$. *Adv. Mater.* **2017**, *29* (18), 1606264.
(39) Lin, J.; Cretu, O.; Zhou, W.; Suenaga, K.; Prasai, D.; Bolotin, K. I.; Cuong, N. T.; Otani, M.; Okada, S.; Lupini, A. R.; Idrobo, J.-C.; Caudel, D.; Burger, A.; Ghimire, N. J.; Yan, J.; Mandrus, D. G.; Pennycook, S. J.; Pantelides, S. T. Flexible Metallic Nanowires with Self-Adaptive Contacts to Semiconducting Transition-Metal Dichalcogenide Monolayers. *Nat. Nanotechnol.* **2014**, *9* (20), 436−442.
(40) Liu, X.; Xu, T.; Wu, X.; Zhang, Z.; Yu, J.; Qiu, H.; Hong, J. H.; Jin, C. H.; Li, J. X.; Wang, X. R.; Sun, L. T.; Guo, W. Top-down Fabrication of Sub-Nanometre Semiconducting Nanoribbons Derived from Molybdenum Disulfide Sheets. *Nat. Commun.* **2013**, *4*, 1776.
(41) Lin, J.; Zhang, Y.; Zhou, W.; Pantelides, S. T. Structural Flexibility and Alloying in Ultrathin Transition-Metal Chalcogenide Nanowires. *ACS Nano* **2016**, *10* (2), 2782−2790.
(42) Le, D.; Sun, D.; Lu, W.; Aminpour, M.; Wang, C.; Ma, Q.; Rahman, T. S.; Bartels, L. Growth of Aligned Mo_6S_6 Nanowires on Cu(111). *Surf. Sci.* **2013**, *611*, 1−4.
(43) Nagata, M.; Shukla, S.; Nakanishi, Y.; Liu, Z.; Lin, Y. C.; Shiga, T.; Nakamura, Y.; Koyama, T.; Kishida, H.; Inoue, T.; Kanda, N.; Ohno, S.; Sakagawa, Y.; Suenaga, K.; Shinohara, H. Isolation of Single-Wired Transition-Metal Monochalcogenides by Carbon Nanotubes. *Nano Lett.* **2019**, *19* (8), 4845−4851.
(44) Yoo, Y.; Jeong, J. S.; Ma, R.; Koester, S. J.; Johns, J. E. Ultrathin One-Dimensional Molybdenum Telluride Quantum Wires Synthesized by Chemical Vapor Deposition. *Chem. Mater.* **2020**, *32* (22), 9650−9655.
(45) Chae, S.; Oh, S.; Siddiqa, A. J.; Choi, K. H.; Lee, W. G.; Jang, W. S.; Lee, J. S.; Kim, Y. M.; Huh, J.; Kim, S. M.; Choi, J. Y. Highly Concentrated Single-Chain Atomic Crystal $LiMo_3Se_3$ Solution Using Ion-Exchange Chromatography. *Chem. Commun.* **2018**, *54* (88), 12503−12506.
(46) Tarascon, J. M. Mo_6Se_6: A New Solid-State Electrode for Secondary Lithium Batteries. *J. Electrochem. Soc.* **1985**, *132*, 2089−2092.
(47) Hönle, W.; Von Schnering, H. G.; Lipka, A.; Yvon, K. New Compounds with Infinite Chains of Face-Condensed Octahedral Mo_6 Clusters: $InMo_3Se_3$, $InMo_3Te_3$, $TlMo_3Se_3$ and $TlMo_3Te_3$. *J. Less-Common Met.* **1980**, *71* (1), 135−145.
(48) Yu, Y.; Wang, G.; Tan, Y.; Wu, N.; Zhang, X. A.; Qin, S. Phase-Controlled Growth of One-Dimensional Mo_6Te_6 Nanowires and Two-Dimensional $MoTe_2$ Ultrathin Films Heterostructures. *Nano Lett.* **2018**, *18* (2), 675−681.
(49) Chevrel, R.; Gougeon, P.; Potel, M.; Sergent, M. Ternary Molybdenum Chalcogenides: A Route to New Extended Clusters. *J. Solid State Chem.* **1985**, *57* (1), 25−33.
(50) Jeon, J.; Oh, S.; Choi, K. H.; Chae, S.; Woo, C.; Dong, X.; Asghar, G.; Ahn, J.; Kim, T. Y.; Ali, J.; Yu, H. K.; Choi, J.-Y. Synthesis of One-Dimensional Atomic Chain $LiMo_3Se_3$ through Ion-Exchange Reaction from $InMo_3Se_3$: Kinetics and Thermodynamics. *Ceram. Int.* **2021**, *47*, 33606.
(51) Murthy, A. P.; Theerthagiri, J.; Madhavan, J.; Murugan, K. Highly Active MoS_2/Carbon Electrocatalysts for the Hydrogen Evolution Reaction − Insight into the Effect of the Internal Resistance and Roughness Factor on the Tafel Slope. *Phys. Chem. Chem. Phys.* **2017**, *19*, 1988−1998.
(52) Vrubel, H.; Moehl, T.; Grätzel, M.; Hu, X. Revealing and Accelerating Slow Electron Transport in Amorphous Molybdenum Sulphide Particles for Hydrogen Evolution Reaction. *Chem. Commun.* **2013**, *49* (79), 8985−8987.
(53) Mei, B. A.; Lau, J.; Lin, T.; Tolbert, S. H.; Dunn, B. S.; Pilon, L. Physical Interpretations of Electrochemical Impedance Spectroscopy of Redox Active Electrodes for Electrical Energy Storage. *J. Phys. Chem. C* **2018**, *122* (43), 24499−24511.
(54) Çakir, D.; Durgun, E.; Gülseren, O.; Ciraci, S. First Principles Study of Electronic and Mechanical Properties of Molybdenum Selenide Type Nanowires. *Phys. Rev. B: Condens. Matter Mater. Phys.* **2006**, *74* (23), 1−8.
(55) Zhang, W.; Wang, J.; Zhao, L.; Wang, J.; Zhao, M. Transition-Metal Monochalcogenide Nanowires: Highly Efficient Bi-Functional Catalysts for the Oxygen Evolution/Reduction Reactions. *Nanoscale* **2020**, *12* (24), 12883−12890.
(56) Zeng, M.; Li, Y. Recent Advances in Heterogeneous Electrocatalysts for the Hydrogen Evolution Reaction. *J. Mater. Chem. A* **2015**, *3* (29), 14942−14962.

https://doi.org/10.1021/acs.iecr.1c02825
Ind. Eng. Chem. Res. 2021, 60, 16153−16161